

Gravitational Lensing of Anisotropic Sources

Rosalba Perna¹ & Charles R. Keeton²

¹*JILA and Department of Astrophysical and Planetary Sciences, University of Colorado, Boulder, CO 80309, USA*

²*Department of Physics and Astronomy, Rutgers University, 136 Frelinghuysen Road, Piscataway, NJ 08854, USA*

Draft 4 November 2018

ABSTRACT

In strong gravitational lensing, the multiple images we see correspond to light rays that leave the source in slightly different directions. If the source emission is anisotropic, the images may differ from conventional lensing predictions (which assume isotropy). To identify scales on which source anisotropy may be important, we study the angle δ between the light rays emerging from the source, for different lensing configurations. If the lens has a power law profile $M \propto R^\gamma$, the angle δ initially increases with lens redshift and then either diverges (for a steep profile $\gamma < 1$), remains constant (for an isothermal profile $\gamma = 1$), or vanishes (for a shallow profile $\gamma > 1$) as $z_l \rightarrow z_s$. The scaling with lens mass is roughly $\delta \propto M^{1/(2-\gamma)}$. The results for an NFW profile are qualitatively similar to those for a shallow power law, with δ peaking at about half the redshift of the source (not half the distance). In practice, beaming could modify the statistics of beamed sources lensed by massive clusters: for an opening angle θ_{jet} , there is a probability as high as $P \sim 0.02\text{--}0.07 (\theta_{\text{jet}}/0.5^\circ)^{-1}$ that one of the lensed images may be missed (for $2 \lesssim z_s \lesssim 6$). Differential absorption within Active Galactic Nuclei could modify the flux ratios of AGNs lensed by clusters; a sample of AGNs lensed by clusters could provide further constraints on the sizes of absorbing regions. Source anisotropy is not likely to be a significant effect in galaxy-scale strong lensing.

Key words: cosmology: gravitational lensing — quasars: absorption lines — galaxies: jets — galaxies: active – gamma rays: bursts

1 INTRODUCTION

In gravitational lensing studies, the emission from the background source is usually assumed to be isotropic such that the appearance of lensed images depends only on the mass distribution in the foreground lensing object and the angular position of the source with respect to the lens. The fluxes of the images can then be written as $F_i = \mu_i F_{\text{src}}$ where μ_i is the lensing magnification at the position of image i , and the source flux F_{src} is assumed to be the same for all images. In this case we can interpret observed flux ratios simply as lensing magnification ratios: $F_j/F_i = \mu_j/\mu_i$. (The one caveat is that if the source is variable, differences in light travel times make it necessary to monitor lensed images and synchronize the light curves in the source time frame before taking the ratio; e.g., Eigenbrod et al. 2005; Kochanek et al. 2006; Fohlmeister et al. 2007, 2008.) The ability to associate flux ratios with magnification ratios underlies many lensing applications, including using anomalous flux ratios to constrain dark matter substructure (e.g., Metcalf & Madau 2001; Chiba 2002; Dalal & Kochanek 2002; Keeton, Gaudi & Petters 2003, 2005; Chiba et al. 2005), and using lens statistics to constrain the mass function and density profiles of galaxies and clusters (e.g., Keeton & Madau 2001;

Kochanek & White 2001; Takahashi & Chiba 2001; Oguri 2002; Ma 2003; Kuhlen, Keeton, & Madau 2004; Oguri & Keeton 2004; Oguri & Blandford 2009)¹

However, many astrophysical sources relevant for gravitational lensing have some degree of anisotropy in their emission. One example is provided by Gamma-Ray Bursters (GRBs).² Numerical simulations (e.g., MacFadyen & Woosley 1999) indicate that the local emissivity is a strong function of the angle that the line of sight makes with the jet axis, and the interpretation of afterglow observations appears to confirm this scenario (Perna, Sari & Frail 2003). Other interpretations instead suggest that the emission is concentrated in a jet with sharp edges and a range of opening angles that can be as small as a degree scale (Nakar, Granot & Guetta 2004). Recent numerical simulations of axisymmetric, magnetically driven outflows (Komissarov et

¹ In lens statistics, the image fluxes are used to determine whether multiple images will be detectable and hence whether systems will be identified as lenses.

² While there are currently no confirmed cases of GRB lensing, the possibility has received considerable attention (e.g., Paczynski 1986; Mao 1992; Grossman & Nowak 1994; Holz et al. 1999; Nemiroff et al. 2000; Porciani & Madau 2001).

al. 2009) have shown that the γ -ray emitting components of GRB outflows magnetically accelerated are very narrow, with $\theta_{\text{jet}} \lesssim 1^\circ$. Furthermore, the GRB emission is highly relativistic, with Lorentz factors $\Gamma \sim 100\text{--}300$ (e.g. Piran 2000). This implies that each point on the emitting surface is only visible to observers within an angle $\theta_{\text{view}} \sim 1/\Gamma \sim 0.2\text{--}0.5$ deg.

Anisotropy in both emission and absorption is also typical of Active Galactic Nuclei (AGNs). The fast TeV variability of the blazars Mrk 501 and PKS 2155-304 was interpreted by Giannios, Uzdensky & Begelman (2009) as the result of compact emitting regions moving with Lorentz factors of $\Gamma \sim 100$ embedded within a jet moving at lower speed. Nair, Jin & Garrett (2005) proposed a helical jet model to explain observations of the gravitationally lensed blazar PKS 1830-211. Even if the emission is intrinsically isotropic, absorption by clouds within the broad line absorption (BAL) region can introduce anisotropy into the net flux out of the source. Indeed, Chelouche (2003) argued that differential absorption along multiple lens sightlines could be detected in spectra of lensed BAL quasars, and Green (2006) suggested that this effect might explain variability in the broad emission lines of only one image of the wide-separation lens SDSS J1004+4112 (Richards et al. 2004). The presence of small-scale structure within the AGN outflow is also supported by numerical simulations (Proga, Stone & Kallman 2000). While the qualitative picture of the BAL region is generally accepted, the quantitative details are still rather uncertain. Debate over the location of BAL clouds spans some five orders of magnitude, $\sim 0.01\text{--}1000$ pc (Elvis 2000; de Kool et al. 2001; Everett, Konigl & Arav 2002). Very little is known about the size of the clouds, although a number of studies suggest an upper limit to the size of $\lesssim 10^{14}$ cm (Baldwin et al. 1995; Elvis 2000; also N. Arav 2009, private communication). A cloud of this size at a distance of a few parsecs would produce differential absorption on a scale of arcseconds.

The key question, then, is whether anisotropy in real astrophysical sources is likely to have a significant impact on observed strong lensing. In order to answer this question, we need to quantify the angle δ between light rays as they leave the source on their way to becoming the multiple images we observe; only anisotropy on a scale $\lesssim \delta$ will be relevant for lensing. In §2 we set up the general problem of lensing of an anisotropic source by a spherical mass distribution. In §3 we study how the angular beam separation δ depends on the lensing configuration for a wide range of lenses with power law mass distributions. In §4 we focus on lenses with the Navarro, Frenk & White (1996) profile. In §5 we use Monte Carlo simulations to compute the distribution of δ angles for a population of NFW clusters. We discuss the implications of our results in §6. We adopt the cosmological parameters $H_0 = 73 \text{ Mpc}^{-1} \text{ km s}^{-1}$, $\Omega_m = 0.24$, and $\Omega_\Lambda = 0.76$ (Spergel et al. 2007).

2 LIGHT BEAM SEPARATION IN MULTIPLY IMAGED SOURCES

Fig. 1 shows a schematic representation of the gravitational lensing geometry with two images, which is generic when the source is sufficiently well aligned with a spherical mass

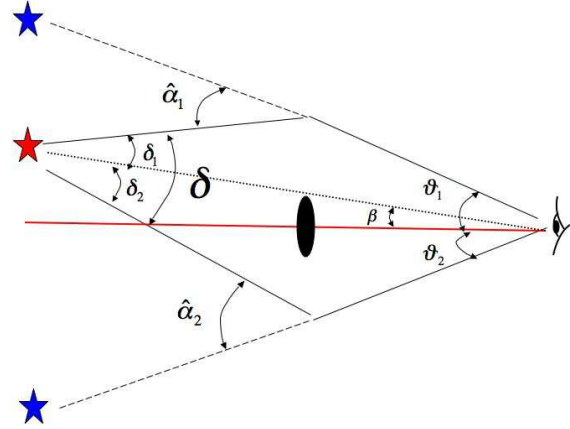


Figure 1. Schematic representation of lensing with two images. A mass profile shallower than isothermal would also have a third image that passes near the galaxy on the opposite side from the source, but such central images are faint and difficult to detect (e.g., Winn et al. 2004) so we focus on the two main, outer images.

distribution. When the central density profile is shallower than isothermal, the image on the opposite side of the lens from the source would be accompanied by a third image that lies closer to the lens galaxy (Burke 1981), but such images are rarely observed (e.g., Winn, Rusin & Kochanek 2004) so in our study we refer to the two outermost images.

As shown in the figure, β is the angular position of the (unlensed) source on the sky with respect to the optical axis (the line connecting the observer and the lens), $\theta_{1,2}$ are the angular positions of the two main images, and the corresponding deflection angles are $\hat{\alpha}_{1,2}$. We are interested in the angle δ between the two light rays that emerge from the source to produce the observed images. This angle can be written as the sum of the angles $\delta_{1,2}$ between the light rays and the line of sight from the observer to the (unlensed) source. Simple geometry allows us to identify these angles as

$$\delta_1 = |\hat{\alpha}_1| - |\theta_1| + \beta, \quad \text{and} \quad \delta_2 = |\hat{\alpha}_2| - |\theta_2| - \beta, \quad (1)$$

so we can express the angular beam separation as

$$\delta = |\hat{\alpha}_1| + |\hat{\alpha}_2| - (|\theta_1| + |\theta_2|). \quad (2)$$

For a spherically symmetric mass distribution, the deflection angle is

$$|\hat{\alpha}(\theta)| = \frac{4GM(\theta)}{c^2 D_1 |\theta|}, \quad (3)$$

where $M(\theta)$ is the projected mass enclosed within angle θ , and D_1 is the angular diameter distance from the observer to the lens, and the sign of the deflection angle is chosen to match the sign of θ . The source and image positions and the deflection angle are linked via the lens equation,

$$\beta = \theta - \frac{D_{\text{ls}}}{D_s} \hat{\alpha}(\theta), \quad (4)$$

where D_s and D_{ls} are angular diameter distances from the observer to the source and from the lens to the source, respectively.

3 POWER LAW MASS DISTRIBUTION

3.1 The lens model

To develop a general understanding of how the angular beam separation depends on the lensing geometry and the physical properties of the lens, we begin with a simple power law mass profile. In length units we write $M(R) = A R^\gamma$ with A some constant, so in angular units we have $M(\theta) = A(D_l\theta)^\gamma$. The cases $\gamma = 0$ and $\gamma = 1$ correspond to the familiar cases of a point mass lens (PM) and a singular isothermal sphere (SIS), respectively. The lens equation takes the form

$$\beta = \theta \mp \theta_E^{2-\gamma} |\theta|^{\gamma-1}, \quad (5)$$

where we use the minus sign when $\theta > 0$ and the plus sign when $\theta < 0$, and the angular Einstein radius is

$$\theta_E = \left(\frac{4GA}{c^2} \frac{D_{ls}}{D_s D_l^{1-\gamma}} \right)^{\frac{1}{2-\gamma}}. \quad (6)$$

Note that if we consider the mass within some fixed physical radius we have $M \propto A$ and hence $\theta_E \propto M^{1/(2-\gamma)}$.

For $0 \leq \gamma < 1$ the lens equation (5) formally has two solutions for all source positions, although when β gets large the image on the opposite side of the lens is faint. For $\gamma = 1$ the lens equation has one or two solutions depending on the position of the source, while for $1 < \gamma < 2$ it has one or three solutions. For each solution, the corresponding deflection angle is given by

$$|\hat{\alpha}(\theta)| = \frac{D_s}{D_{ls}} \theta_E^{2-\gamma} |\theta|^{\gamma-1}. \quad (7)$$

3.2 The angular beam separation

As we study how the angular beam separation depends on the lens redshift z_l , we want to keep the *physical* properties of the lens fixed, which is why we elected to write the mass profile as $M = A R^\gamma$ where A is a constant. To facilitate the comparison of models with different power law slopes γ , we choose the value of A such that the different masses all have the same Einstein radius when the lens is halfway between the observer and source.

Fig. 2 shows the angular beam separation as a function of lens redshift for a point mass lens ($\gamma = 0$), considering two values of the source redshift and different values of the angle β of the source with respect to the optical axis. A striking result is the steep increase of δ with z_l . This and other scalings can be understood as follows. The two images are located at the angular positions $\theta_{1,2} = (\beta \pm \sqrt{4\theta_E^2 + \beta^2})/2$, and the corresponding deflection angles are $\hat{\alpha}_{1,2} = (D_s/D_{ls}) \theta_E^2/\theta_{1,2}$. Equation (2) then yields

$$\delta_{PM} = \left(\frac{D_s}{D_{ls}} - 1 \right) \sqrt{4\theta_E^2 + \beta^2}. \quad (8)$$

This equation elucidates the trends apparent in the figure. First, since $\theta_E^{PM} \propto D_{ls}^{1/2}$ we see that δ_{PM} formally diverges³ as the lens approaches the source ($z_l \rightarrow z_s$ and hence $D_{ls} \rightarrow 0$). This divergence occurs for all values of the source angle β . Second, it is clear that $\delta_{PM} \rightarrow 0$ as the lens approaches the

observer ($z_l \rightarrow 0$ and $D_{ls} \rightarrow D_s$). Third, when the source and lens redshifts and the lens mass are all fixed, δ_{PM} increases with β . Fourth, when the source is well aligned with the lens ($\beta \ll \theta_E$), the angular beam separation scales with the lens mass as $\delta_{PM} \propto M^{1/2}$. Finally, in the opposite limit in which $\beta \gg \theta_E$, δ_{PM} becomes independent of the mass of the lens (although this particular case is perhaps less relevant than the others because when $\beta \gg \theta_E$ the counter-image is faint).

Fig. 3 shows the results for other power law profiles, including one that is extended but steeper than isothermal ($\gamma = 0.5$), the isothermal profile ($\gamma = 1$), and one shallower profile ($\gamma = 1.5$). For all cases we fix $\beta = 10^{-4}$ deg, which is small enough that we are always looking at situations with multiple images. As we shall see, for shallow profiles the angular beam separation is not very sensitive to the choice of β .

Qualitatively, steep profiles ($\gamma < 1$) behave in a similar way as the point mass case, with δ increasing monotonically with z_l and diverging as the lens nears the source. In these cases we find that δ increases with the source position β (the case $\gamma = 0$ is shown in Fig. 2; the case $\gamma = 0.5$ is not shown).

The isothermal profile ($\gamma = 1$) represents a transition case, with δ increasing monotonically with the lens redshift and reaching a finite value as $z_l \rightarrow z_s$. This is another case we can understand analytically. For $\beta < \theta_E$ there are two images at positions $\theta_{1,2} = \theta_E \pm \beta$. Combining these with the deflection angles $\hat{\alpha}_{1,2} = (D_s/D_{ls}) \theta_E$ yields the angular beam separation

$$\delta_{SIS} = 2\theta_E \left(\frac{D_s}{D_{ls}} - 1 \right). \quad (9)$$

An SIS has $\theta_E \propto D_{ls}$, so when $z_l \rightarrow z_s$ we see that δ approaches a constant. Another general point is that δ is independent of β , while depending linearly on the mass of the lens ($\delta_{SIS} \propto \theta_E \propto M$, where we are considering the mass within some fixed physical radius; cf. §3.1).

Profiles shallower than isothermal ($\gamma > 1$) show a qualitatively different behaviour: as z_l increases, the angular beam separation δ initially rises but then reaches a peak before turning over and returning to zero as $z_l \rightarrow z_s$. While there is no simple, general expression for δ as a function of both the power law slope γ and source position β , we can find an enlightening analytic result for the limit $\beta \ll \theta_E$. In this case the images are near the Einstein radius, $\theta_{1,2} \approx \theta_E$, so the two deflections angles are $\hat{\alpha}_{1,2} \approx D_s/D_{ls} \theta_E$, and we have $\delta \approx 2\theta_E (D_s/D_{ls} - 1)$. Then, for $D_{ls} \rightarrow 0$ we have $\theta_E \propto D_{ls}^{1/(2-\gamma)}$ and hence

$$\delta \propto D_{ls}^{1/(2-\gamma)} \left(\frac{D_s}{D_{ls}} - 1 \right) \rightarrow D_{ls}^{(\gamma-1)/(\gamma-2)}. \quad (10)$$

This result clarifies the distinction between steep and shallow profiles: as the lens nears the source, δ diverges for all $\gamma < 1$, approaches a constant for $\gamma = 1$, and vanishes for all $\gamma > 1$. Finally note that in this limit when β is small we have the following scaling with lens mass: $\delta \propto \theta_E \propto M^{1/(2-\gamma)}$.

While we have explicitly shown results for a single value of the angular source position β , we find that the general behaviour of δ with lens redshift and mass holds for other values as well. We have demonstrated this analytically for the cases of $\gamma = 0$ and $\gamma = 1$. More generally, for steep profiles ($\gamma < 1$), which have two images for all β , we find that the rise of δ becomes increasingly steep as β becomes

³ In practice the small-angle approximation would break down before δ truly diverges.

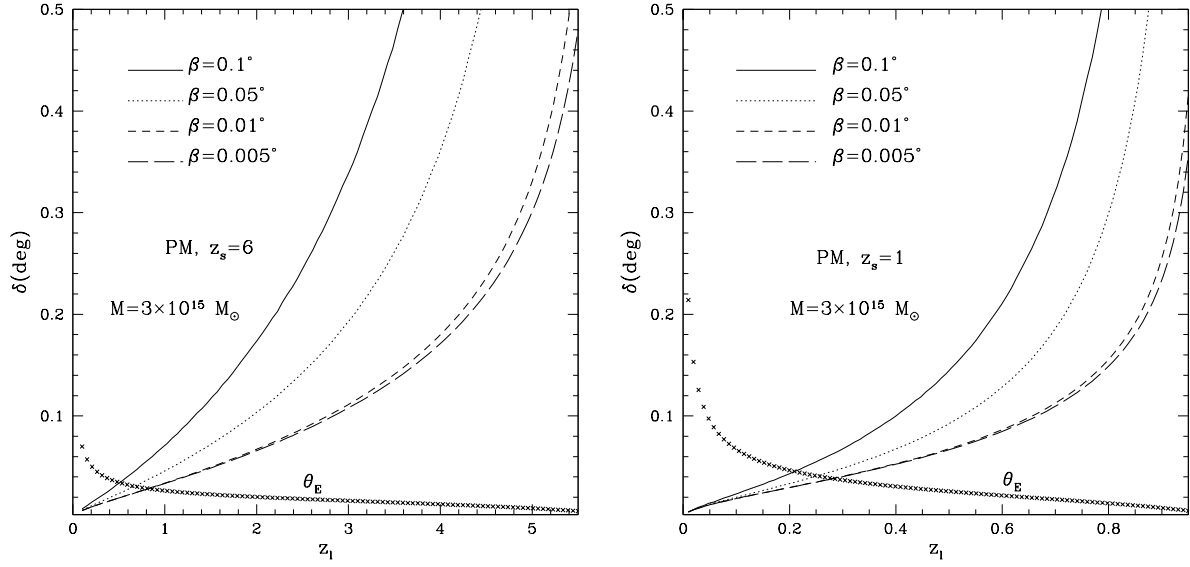


Figure 2. The angular beam separation δ for a point mass lens as a function of the lens redshift. Different curves correspond to different source positions. The lens mass is $M = 3 \times 10^{15} M_{\odot}$ and the source redshift is $z_s = 6$ (left panel) and $z_s = 1$ (right panel). The points near the bottom of each panel show the Einstein radius as a function of the lens redshift.

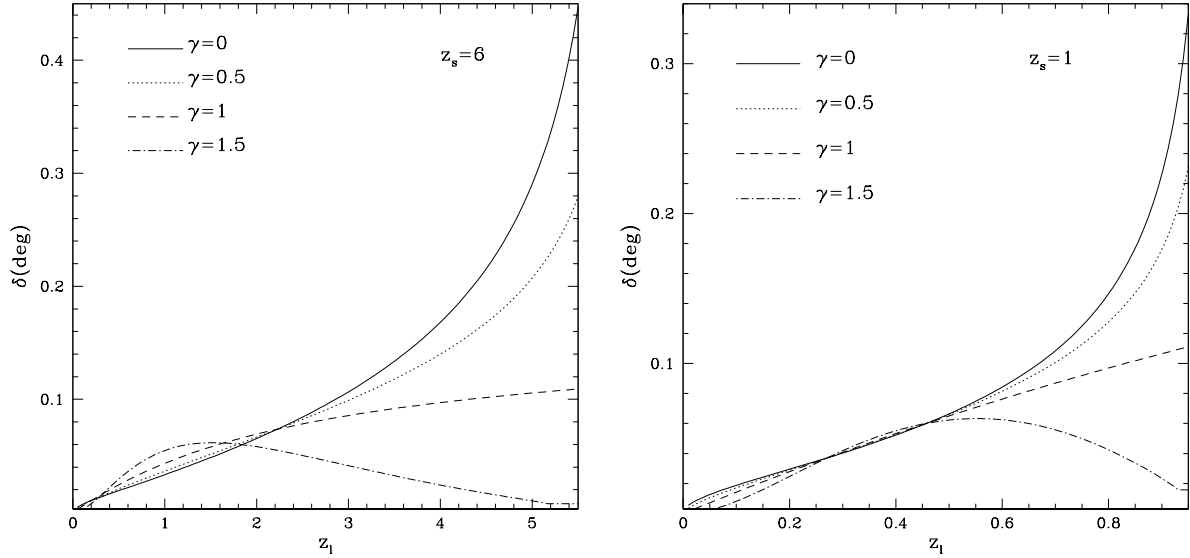


Figure 3. The angular beam separation δ for a lens with a power law mass distribution $M = A(D_l \theta)^\gamma$, as a function of the lens redshift. Different curves correspond to different power law slopes. The point mass case ($\gamma = 0$) has a mass of $M = 3 \times 10^{15} M_{\odot}$, while in the other cases the mass normalization A is fixed so that all lenses have the same Einstein radius when $D_l = D_s/2$. The source redshift is $z_s = 6$ (left panel) and $z_s = 1$ (right panel). We fix the source position $\beta = 10^{-4}$ deg, but note that for $\gamma \leq 1$ the dependence of δ on β is negligible.

larger than θ_E . For shallow profiles ($\gamma > 1$), by contrast, there are two images only when β is sufficiently small that the source lies inside the lens caustic, and it turns out that the dependence of δ on β is quite weak.

4 NAVARRO-FRANK-WHITE MASS DISTRIBUTION

4.1 The lens model

The NFW profile (Navarro, Frank & White 1996),

$$\rho(r) = \frac{\rho_s}{(r/r_s)(1 + r/r_s)^2}, \quad (11)$$

is fully specified by two parameters, written here as a scale radius r_s and characteristic density ρ_s . It is customary to trade these two parameters for the (virial) mass M_{vir} and concentration c . The transformation goes by way of the virial radius r_{vir} , which is related to the virial mass by $M_{\text{vir}} = (4\pi/3)\Delta_{\text{vir}}\bar{\rho}r_{\text{vir}}^3$, where Δ_{vir} is the virial overdensity, and the mean matter density is $\bar{\rho}(z) = 3H_0^2\Omega_m(1+z)^3/8\pi G$. For the virial overdensity we use the fitting formula provided by Bullock et al. (2001): $\Delta_{\text{vir}} \approx (18\pi^2 + 82x - 39x^2)/\Omega(z)$, where $x \equiv \Omega(z) - 1$, and $\Omega(z)$ is the ratio of the mean matter density to the critical density at redshift z . Using these ingredients, we can finally specify the original NFW parameters: $r_s = r_{\text{vir}}/c$, and $\rho_s = \delta_c \bar{\rho}$, and

$$\delta_c(z) = \frac{\Delta_{\text{vir}}(z)}{3} \frac{c^3}{[\ln(1+c) - c/(1+c)]}. \quad (12)$$

The two NFW parameters are not entirely independent: numerical simulations reveal a relation between the mass and concentration of NFW halos. Bullock et al. (2001) describe this relation as a log-normal distribution for the concentration whose median value depends on the halo mass and redshift,

$$c_{\text{med}}(M, z) = \frac{\bar{c}_s}{1+z} \left(\frac{M}{M_*} \right)^\alpha, \quad (13)$$

where M_* is the mass of a typical halo collapsing today. For a cosmology with $\sigma_8 = 0.9$ and $w = -1$, $M_* = 1.13 \times 10^{13} M_\odot$ (Kuhlen, Keeton & Madau 2004). The halos in the Λ CDM simulations by Bullock et al. were best described by the parameter values $\bar{c}_s = 9.0$ and $\alpha = -0.13$. Although the simulations show a scatter, for simplicity we just use the median concentration at each mass and redshift.

The lensing characteristics of an NFW halo are given by Bartelmann (1996). The projected surface mass density, scaled by the critical density for lensing, is

$$\kappa(x) = 2\kappa_s \frac{f(x)}{x^2 - 1}, \quad (14)$$

where $x \equiv r/r_s$,

$$f(x) = \begin{cases} 1 - \frac{2}{\sqrt{x^2-1}} \arctan \sqrt{\frac{x-1}{x+1}} & \text{if } x > 1 \\ 1 - \frac{2}{\sqrt{1-x^2}} \operatorname{arctanh} \sqrt{\frac{1-x}{x+1}} & \text{if } x < 1 \\ 0 & \text{if } x = 1 \end{cases} \quad (15)$$

and $\kappa_s \equiv \rho_s r_s \Sigma_{\text{crit}}^{-1}$ is a characteristic surface mass density in units of the critical density for lensing,

$$\Sigma_{\text{crit}} = \frac{c^2}{4\pi G} \frac{D_s}{D_1 D_{\text{ls}}}. \quad (16)$$

The (scaled) mass inside radius x is

$$m(x) = 2 \int_0^x dx' x' \kappa(x') = 4\kappa_s g(x), \quad (17)$$

where $g(x) = \log(x/2) + 1 - f(x)$. With this notation, we can write the lens equation in scaled coordinates as

$$y = x - \frac{4\kappa_s g(|x|)}{x}, \quad (18)$$

where $y = \beta/\theta_0$ is the source angle scaled by the angular NFW scale radius, $\theta_0 = r_s/D_1$. An NFW lens has one tangential and one radial critical curve, whose scaled radii x_t and x_r are given by the solutions of the equations

$$1 - \frac{m(x)}{x^2} \Big|_{x=x_t} = 0, \quad 1 - \frac{d}{dx} \frac{m(x)}{x} \Big|_{x=x_r} = 0. \quad (19)$$

The tangential critical curve maps to the origin in the source plane (i.e., it represents the Einstein ring), while the radial critical curve maps to the caustic in the source plane, which has angular radius $y_{\text{caus}} = m(x_r)/x_r - x_r$. If $y < y_{\text{caus}}$, an NFW lens produces three images: one of the main images is outside x_t , the other is between x_t and x_r , and the third image (the one we ignore) is inside x_r . All of these scaled variables can be converted into angular variables by multiplying by θ_0 .

For an image at angular position θ , the deflection angle is

$$|\hat{\alpha}(\theta)| = \frac{D_s}{D_{\text{ls}}} \frac{m(|\theta|/\theta_0)}{|\theta|/\theta_0} \theta_0. \quad (20)$$

4.2 The angular beam separation

Fig. 4 shows the angular beam separation δ as a function of lens redshift for certain values of the lens mass and source redshift. From a qualitative point of view, the curves resemble the curve for the shallow power law case in Fig. 3. This is not surprising, since the NFW profile is shallower than isothermal inside the scale radius r_s , and the Einstein radius is (much) less than the scale radius for all cases of interest.

The $\delta(z_l)$ curves peak at a redshift which is about half that of the source. This is curious but coincidental; it arises from the different redshift dependences of the image positions and deflection angles. Fig. 5 shows δ along with its four constituents: the image positions $\theta_{1,2}$ and deflection angles $\hat{\alpha}_{1,2}$. (These are plotted in units of θ_0 , but that scale factor has a weak dependence on z_l .) Neither the image position curves nor the deflection angle curves peak at $\sim z_s/2$; the image position curves peak at lower redshift, in keeping with the rule of thumb that a lens is most effective when it is about half the *distance* to the source. As far as we can tell, it is purely coincidental that the different redshift dependences cause the peak of the δ curve to be located at $\sim z_s/2$.

Another interesting point from Fig. 5 is that the angular beam separation is quite insensitive to the source position even though its constituents do depend on β . This is because the image position and deflection angle depend on β in a similar way: as β increases, θ_1 and $\hat{\alpha}_1$ both increase while θ_2 and $\hat{\alpha}_2$ both decrease (in amplitude). The way these terms combine to form the angular beam separation means the changes largely cancel and leave δ relatively insensitive to β .

To illustrate one way of interpreting the δ values, let us consider lensing of a beamed source. Depending on the angular beam separation δ and the jet opening angle⁴ θ_{jet} , there may be configurations in which we see only a single image even though conventional lens theory (which assumes an isotropic source) would predict two. For example, in the limit that the angular beam separation is larger than the jet opening angle ($\delta > \theta_{\text{jet}}$), there is no way to arrange the

⁴ We take θ_{jet} to be the full opening angle, i.e., from one side of the jet to the other.

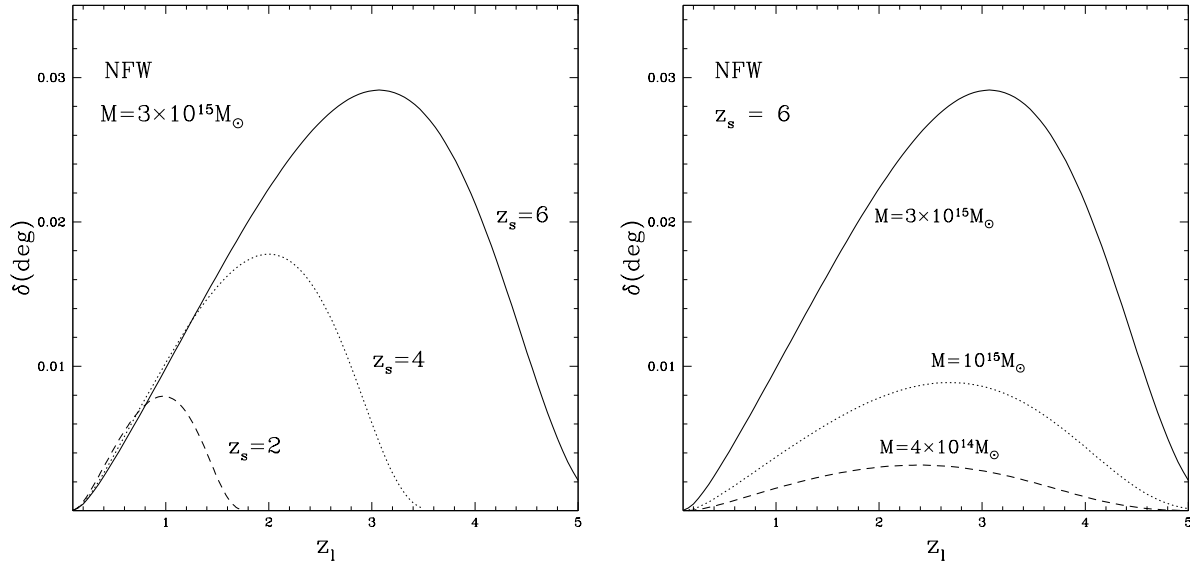


Figure 4. The angular beam separation δ as a function of lens redshift for an NFW lens with three different source redshifts (*left panel*) and three different lens masses (*right panel*). The source position is taken to be $\beta = 0.05\beta_{\text{caus}}$, but δ is not very sensitive to this choice.

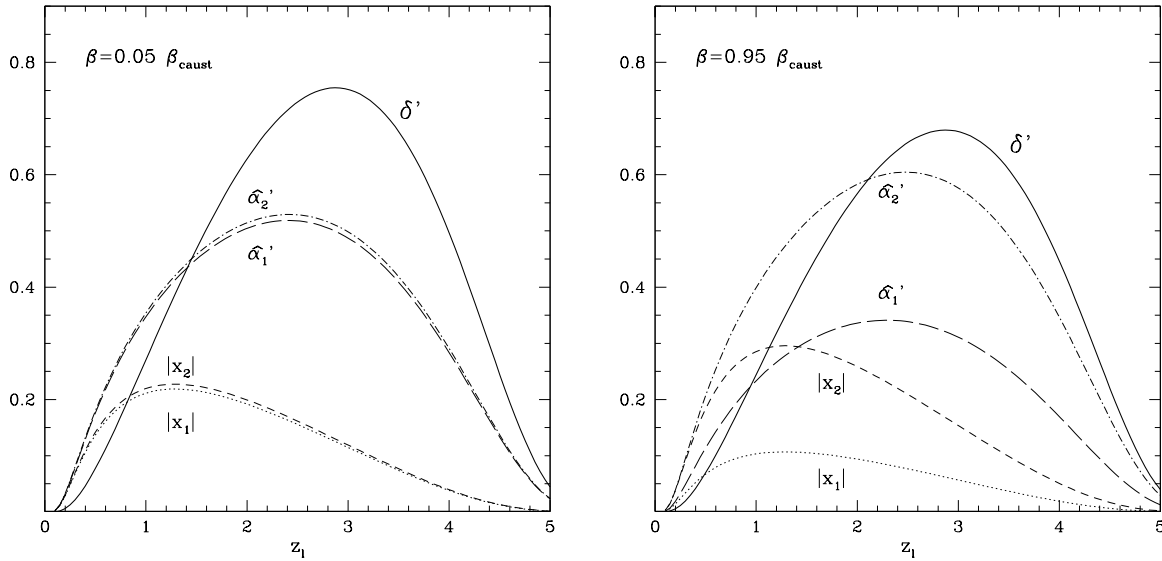


Figure 5. Image positions ($x_{1,2}$), deflections angles ($\hat{\alpha}_{1,2}$) and angular beam separation (δ) for an NFW lens. All quantities are in units of θ_0 (the ‘prime’ distinguishes them from the corresponding quantities in angular units). The lens mass is $M = 3 \times 10^{15} M_\odot$, and the source redshift is $z_s = 6$. In the left panel the source is close to the optical axis ($\beta = 0.05\beta_{\text{caus}}$), while in the right panel it is close to the caustic ($\beta = 0.95\beta_{\text{caus}}$). Note that the image positions and deflection angles depend on the source position, but the angular beam separation δ is almost independent of β .

jet such that we could see both images: we could see one image or the other, or nothing at all (if the jet does not point along either light ray), but never both images. In this case the probability that we would “miss” one of the images predicted by conventional lens theory is unity.

For $\delta < \theta_{\text{jet}}$ there is some finite probability of missing one of the images. Given δ and θ_{jet} , we use simple numerical simulations to consider all possible jet orientations and compute the conditional probability that one image is

missed, given that at least one image is seen. (The conditional part of the probability just means we do not consider cases where the jet is pointing “away” from us so that we cannot see anything.) The results are shown in Fig. 6. In the limit $\delta \ll \theta_{\text{jet}} \ll 1$ we can derive a useful analytic approximation $P \approx (4\delta)/(\pi\theta_{\text{jet}})$, which is also shown in the figure. Combining the probability results with the δ values from Fig. 4, we deduce that there is some finite probability that a beamed source could be “lensed” by a massive NFW cluster

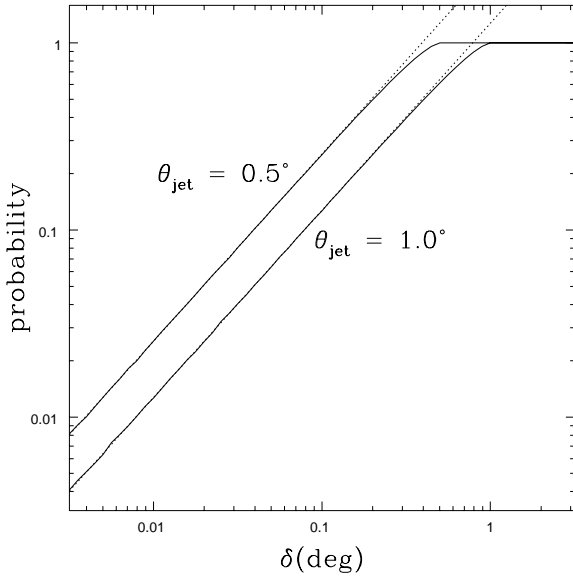


Figure 6. For a beamed source with opening angle θ_{jet} , the solid curves show the probability that one of the lensed images is missed, given that at least one image is seen, as a function of the angular beam separation δ . The probability saturates at unity for $\delta \geq \theta_{\text{jet}}$ (see text). The dotted lines show the approximation $P \approx (4\delta)/(\pi\theta_{\text{jet}})$.

in such a way that we miss one of the images, and that this probability could be as high as $P \sim 0.02\text{--}0.07 (\theta_{\text{jet}}/0.5^\circ)^{-1}$ depending on the redshift of the source. This probability is largest when $z_1 \sim z_s/2$. (By contrast, the corresponding probability for a steep power law mass profile would become ever larger as $z_1 \rightarrow z_s$.)

5 COSMOLOGICAL POPULATION OF NFW LENSES

The effects of source anisotropy depend on the angular beam separation, which in turn depend on the redshift, mass, and profile of the lens. For a lens system in which the lensing galaxy or cluster is known, it would be natural to study source anisotropy using the specific lens configuration. But for a system in which the lensing object has not yet been identified, it would be important to understand the statistical distribution of angular beam separations. We now examine that distribution using Monte Carlo simulations of a population of halos between the observer and source. Since we have seen that the angular beam separation is largest for massive lenses (which is not surprising), we focus on cluster lenses here. We treat the clusters using the NFW profile, which of course is oversimplified but serves to give useful first estimates.

We model the cluster population using the mass function from Warren et al. (2006),

$$n(M, z) = 0.7234 \left(\sigma_M^{-1.625} + 0.2538 \right) e^{-1.1982/\sigma_M^2} \times \frac{\hat{\rho}(z)}{M^2} \frac{d \log \sigma_M^{-1}}{d \log M}, \quad (21)$$

where $\hat{\rho}(z)$ is the mean comoving matter density at redshift z , and σ_M is the linear density fluctuation on mass scale M . In terms of the power spectrum, $\sigma_M^2 = (1/2\pi^2) \int dk k^2 P(k) W(kR)^2$, where $P(k)$ is the matter power spectrum, $W(kR)$ is the window function corresponding to the smoothing of the density field (e.g., Peebles 1993), and R is the comoving scale corresponding to a mass $M = (4\pi/3)\bar{\rho}R^3$.

Let us now consider a source at redshift z_s . The probability that its light is (multiply) lensed by a mass on its way to the observer, is given by the fraction of the sky that is covered by lens caustics:⁵

$$P_{\text{lens}} = \frac{1}{4\pi} \int \int f(M, z) dM dz, \quad (22)$$

where

$$f(M, z) = \pi \beta_{\text{caus}}^2 n(M, z) \frac{dV}{dz}(z), \quad (23)$$

and $dV/dz(z)$ is the comoving volume at redshift z . We can interpret $f(M, z)$ (once it is normalized) as the joint probability distribution for the halo mass and redshift, and draw from this distribution as follows. First, we obtain the redshift distribution by marginalizing over mass: $P'_{\text{lens}}(z) = A_1 \int_{M_{\text{min}}}^{M_{\text{max}}} f(M, z) dM$, where A_1 is a normalization factor. We consider the mass range from $M_{\text{min}} = 10^{14} M_\odot$ to $M_{\text{max}} = 3 \times 10^{15} M_\odot$. As we shall see, reducing the minimum mass would principally affect the distribution of angular beam separations at the small- δ end, which is not so interesting from the standpoint of expected anisotropy scales. Our results are not very sensitive to the upper mass cut because higher mass halos are exponentially rare. We draw a random lens redshift z_1 from $P'_{\text{lens}}(z)$, and then construct the conditional probability distribution for the mass: $P''_{\text{lens}}(M|z_1) = A_2 f(M, z_1)$, where A_2 is again a normalization factor. Note that the factor of $\pi \beta_{\text{caus}}^2$ in eq. (23) ensures that each halo is weighted by its lensing cross section.

Once we have drawn a lens mass and redshift, we need to draw a random source position. Since we consider only multiply-imaged sources, we can restrict attention to $0 \leq \beta \leq \beta_{\text{caus}}$. We assume a uniform distribution of source positions (in 2-d), which is equivalent to $P(\beta) d\beta = (2\beta/\beta_{\text{caus}}^2) d\beta$. We note that lensing magnification bias can cause the distribution of source positions to be non-uniform. However, since the angular beam separation for NFW lenses is not very sensitive to β (even for β on or near a caustic; cf. §4.2), our results are not very sensitive to the distribution of source positions.

For each set of (z_1, M, β) values we compute the angular beam separation δ , and then repeat the process many times to obtain the δ distribution. Fig. 7 shows the results. In analyzing the results, we examine one case in which we consider all halos above a fixed mass threshold (left panel of Fig. 7), and a second case in which we consider all halos

⁵ If we were considering a particular flux-limited survey, we would need to consider not only the fraction of the sky covered by caustics (the lensing optical depth) but also the fact that lensing configurations with higher magnifications are easier to detect (magnification bias). We find, though, that magnification bias does not significantly affect our conclusions about the distribution of δ values.

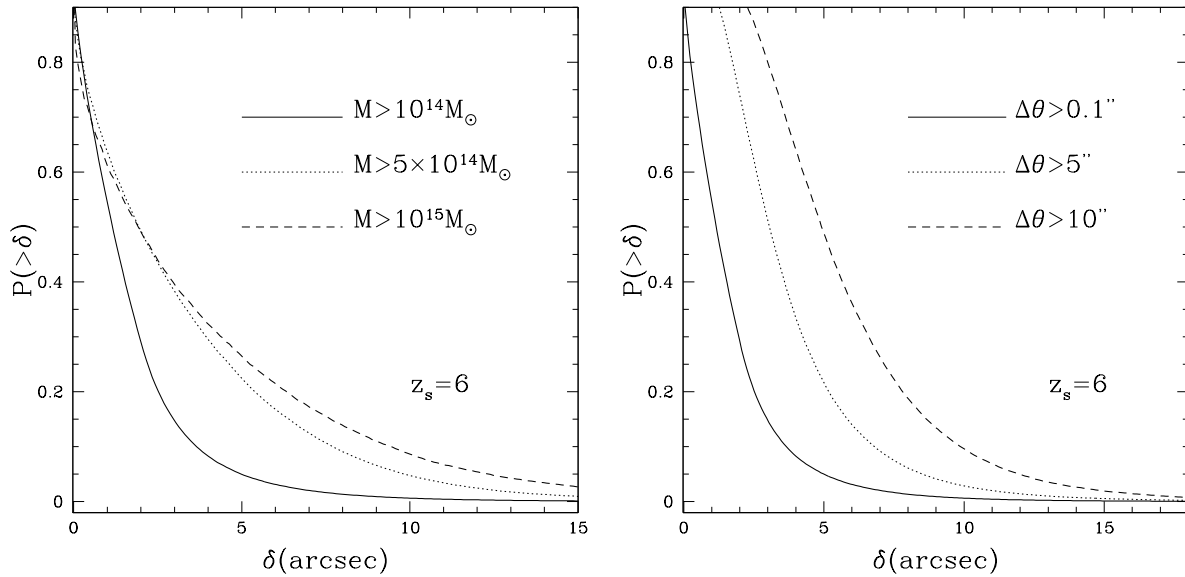


Figure 7. Cumulative probability distribution for a lensed source at redshift $z_s = 6$ to have an angular beam separation greater than δ . The left panel shows results for different mass cuts, while the right panel shows results for different image separation cuts.

that produce a lens image separation larger than some value (right panel).

The range of δ values typical for the statistical distribution is somewhat smaller than the values seen in Fig. 4, which is not surprising because the cluster population tends to be dominated by clusters at lower masses and redshifts than were used for the previous example, and both effects tend to reduce δ . A useful corollary is that, since $\delta(z_l)$ is largely insensitive to z_s (see the left panel of Fig. 4), the δ distributions shown in Fig. 7 are not very dependent upon the assumed source redshift.

The typical value of δ increases with the mass or image separation threshold, which is also not surprising. If we consider wide-separation lenses with $\Delta\theta > 10''$, the median angular beam separation is $\delta \approx 5''$, and there is about a 10% chance that the angular beam separation would be larger than about $10''$. As discussed below, this range of δ values corresponds to possible scales of anisotropy in real astrophysical sources, which suggests that source anisotropy may have non-negligible if not dominant effects in strong lensing.

6 SUMMARY AND DISCUSSION

Motivated by the observation that anisotropic emission is ubiquitous in astrophysical sources, we have addressed the general problem of gravitational lensing of an anisotropic source. For simplicity, in this pilot study we have focused on spherical mass distributions.

The slope of the mass profile plays a crucial role in determining the angular beam separation δ between the two main lensed images, and hence the probability that the appearance of the images will be affected by source anisotropy (that we might miss one of the images of a beamed source, for example). If the mass profile is steeper than isothermal, δ increases with the redshift of the lens (for a fixed source redshift). If the mass profile is shallower than isothermal, δ

peaks when the lens is somewhere in between the observer and the source. In the case of an NFW lens, the peak occurs for $z_l \sim z_s/2$. In general, the angular beam separation δ is not necessarily similar to the image separation, $\Delta\theta$.

By modeling a cosmological distribution of clusters with NFW profiles, we have estimated the distribution of angular beam separations—and, by implication, the range of source anisotropy scales that are most likely to affect lensing. Typical values of δ for cluster lenses lie in the range of a few to tens of arcseconds. We remark that while our statistical analysis should be instructive, there are some complications we have omitted in this pilot study. If baryons steepen the central density profile (compared with the pure NFW profiles we have considered; see Puchwein et al. 2005; Rozo et al. 2008), that would tend to increase the δ values. In general we would expect asphericity to change δ only by a factor of order unity, although that would introduce some new phenomenology in terms of how source anisotropy would affect lenses with more than two bright images corresponding to more than two light rays emerging from the source.

Our results have implications for a range of astrophysical sources. Gamma-Ray Bursts are known to be extremely relativistic sources, with Lorentz factors $\Gamma \sim 100$ –300. This implies that each point on the emitting surface is only visible to observers within a sub-degree scale. If the GRB emitting region is confined within a region $\lesssim 1^\circ$ (as suggested by recent numerical simulations; Komissarov et al. 2009), GRBs would be excellent candidates to display effects of anisotropic lensing. Since GRBs are short-lived sources, GRB lensing would not generally result in contemporaneous multiple imaging. Rather, if a GRB goes off behind a massive cluster, one would naively expect to see a nearly identical (modulo some magnification factor) GRB within the same instrumental error circle some months or years later. We have found, however, that there could be a small but finite probability that one of the images could be missed because of the angular beam separation between the light

rays that form the lensed images. As a specific example, if we consider a GRB at $z_s = 6$ lensed by a massive cluster at $z_l = 1$ (i.e., the scenario depicted in Fig. 4), and its jet opening angle is $\theta_{\text{jet}} = 1^\circ$, there is a 1% probability that the second GRB image will not appear. That probability doubles if $\theta_{\text{jet}} = 0.5^\circ$, and it increases to about 6% for a lens redshift $z_l = 3$. The possibility of missing images ought to be incorporated into statistical forecasts of GRB lensing (which have heretofore assumed isotropic source emission; cf. Porciani & Madau 2001).

Other sources that have been suggested to be highly relativistic are blazars. Giannios et al. (2009) suggested that the fast TeV variability observed in two sources can be explained as the result of compact emitting regions moving towards the observer with Lorentz factors of ~ 100 , and embedded within a jet moving at lower speed. In this scenario, the emission from each blob is beamed within a sub-degree scale. Depending on the angle at which the blob is moving with respect to the line of sight to the observer, there is some probability that a lensed blazar might be missing one of the images. If that does happen to be the case in lensing observations (e.g., when a blazar is observed behind a large cluster and the number of images appears anomalous) it would provide support for this physical picture of blazars.

Anisotropy in the net flux leaving the source can also result from inhomogeneous absorption within the source. This is indeed the case for AGNs, in which dense clouds in the broad absorption line region create a highly anisotropic absorption pattern. The precise location and size of these clouds is still a controversial issue. Estimates suggest that their size is not larger than about 10^{14} cm (e.g., Baldwin et al. 1995; Elvis 2000), while their location has been placed in a range between 0.01 and 1000 pc (e.g., de Kool et al. 2001; Everett et al. 2002). These scales fall in a quite interesting range for our problem. A cloud of size 10^{14} cm at a distance of 1 pc would subtend an angle of about $7''$, which is similar to the median angular beam separation for NFW lenses with image separations $\Delta\theta > 10''$. If the cloud were significantly closer to the central engine than 1 pc, it would most likely cover both of the light rays that correspond to lensed images, so the importance of source anisotropy would depend on whether there is significant internal structure within BAL clouds on scales smaller than 10^{14} cm. Conversely, if BAL clouds are significantly farther than 1 pc, the importance of source anisotropy would depend on the covering fraction of BAL clouds.

If an AGN is strongly lensed and there is significant differential absorption within the source, that would effectively cause different lensed images to have different source fluxes, which would in turn break the connection between observed flux ratios and lensing magnification ratios. If this complication is not recognized, it could lead to errors in lens models and their interpretation. By contrast, if the differential source absorption is recognized, the ability to simultaneously probe multiple lines of sight into the source with strong lensing would provide a new way to probe the structure of the absorbing medium in AGN, which is still very uncertain. This possibility is related to the suggestion by Chelouche (2003) and Green (2006) that lensed quasars can be used to study small-scale structure in quasar outflows. One good way to identify differential absorption would be to compare flux measurements at both X-ray and op-

tical wavelengths (Green 2006). Column densities inferred for the absorbers in the broad line regions are $N_{\text{H}} \gtrsim 10^{22}$ cm $^{-2}$, much larger than derived from the UV (Green et al. 2001; Gallagher et al. 2002). Therefore, one expects that a light ray passing through an absorber would have a smaller X-ray/optical flux ratio than a non-absorbed ray.

In summary, anisotropy in sources that are gravitationally lensed could influence the appearance of the lensed images—including whether we even see all the images. The effect will be most significant for wide-separation lenses produced by cluster-mass objects. Source anisotropy will probably not dramatically alter the statistics of GRBs, blazars, and AGNs lensed by clusters, but its effect may be non-negligible and certainly ought to be considered. If effects of source anisotropy can be recognized, they would provide a unique opportunity to learn more about the small-scale structure of the emitting region of the source.

ACKNOWLEDGEMENTS

We thank Nahum Arav for discussions on absorbers in AGNs, Elena Pierpaoli for discussions on clusters, and Kelly Wieand for discussions about the jet probability calculation. CRK acknowledges support from NSF through grant AST-0747311.

REFERENCES

- Baldwin, J., Ferland, G., Korista, K., Verner, D. 1995, *ApJ*, 455, L119
- Bartelmann, M. 1996, *A&A*, 313, 697
- Bullock, J. S., Kolatt, T. S., Sigad, Y., Somerville, R. S., Kravtsov, A. V., Klypin, A. A., Primack, J. R., Dekel, A. 2001, *MNRAS*, 321, 559
- Burke, W. L., 1981, *ApJ*, 244, L1
- Chelouche, D. 2003, *ApJ*, 596, L43
- Chiba, M. 2002, *ApJ*, 565, 17
- Chiba, M., Minezaki, T., Kashikawa, N., Kataza, H., & Inoue, K. T. 2005, *ApJ*, 627, 53
- Dalal, N., & Kochanek, C. S. 2002, *ApJ*, 572, 25
- de Kool, M., Arav, N., Becker, R. H., Gregg, M. D., White, R. L., Laurent-Muehleisen, S. A., Price, T., Korista, K. T. 2001, *ApJ*, 548, 609
- Eigenbrod, A., Courbin, F., Vuissoz, C., Meylan, G., Saha, P., & Dye, S. 2005, *A&A*, 436, 25
- Elvis, M. 2000, *ApJ*, 545, 63
- Everett, J., Konigl, A., & Arav, N. 2002, *ApJ*, 569, 671
- Fohlmeister, J., et al. 2007, *ApJ*, 662, 62
- Fohlmeister, J., Kochanek, C. S., Falco, E. E., Morgan, C. W., & Wambsganss, J. 2008, *ApJ*, 676, 761
- Gallagher, S. C., Brandt, W. N., Wills, B. J., Charlton, J. C., Chartas, G., Laor, A. 2004, *ApJ*, 603, 425
- Green, P. J. et al. 2001, *ApJ*, 558, 109
- Green, P. J. 2006, *ApJ*, 644, 733
- Grossman, S. A., & Nowak, M. A. 1994, *ApJ*, 435, 548
- Holz, D. E., Miller, M. C., & Quashnock, J. M. 1999, *ApJ*, 510, 54
- Keeton, C. R., Gaudi, B. S., & Petters, A. O. 2003, *ApJ*, 598, 138
- Keeton, C. R., Gaudi, B. S., & Petters, A. O. 2005, *ApJ*, 635, 35
- Keeton, C. R., & Madau, P. 2001, *ApJ*, 549, L25
- Kochanek, C. S., & White, M. 2001, *ApJ*, 559, 531
- Kochanek, C. S., et al. 2006, *ApJ*, 640, 47
- Komissarov, S. S., Vlahakis, N. K., Konigl, A., & Barkov, M. V. 2009, *MNRAS* in press

- Kuhlen, M., Keeton, C. R., Madau, P. 2004, *ApJ*, 601, 104
Ma, C.-P. 2003, *ApJ*, 584, L1
MacFadyen, A. I. & Woosley, S. E. 1999, *ApJ*, 524, 262
Mao, S. 1992, *ApJ*, 389, L41
Metcalf, R. B., & Madau, P. 2001, *ApJ*, 563, 9
Nair, S., Jin, C., Garrett, M. A. 2005, *MNRAS*, 362, 1157
Nakar, E., Granot, J., Guetta, D. 2004, *ApJ*, 606L, 37
Navarro, J., Frank & White, S. 1996, *ApJ*, 62, 563
Nemiroff, R. J., Marani, G. F., Norris, J. P., Bonnell, J. T., Mee-
gan, C. A., & Hurley, K. C. 2000, in *Gamma-Ray Bursts: 5th
Huntsville Symposium* (AIP Conf. Proc. Vol. 526), p. 663
Oguri, M. 2002, *ApJ*, 580, 2
Oguri, M. & Keeton, C. R. 2004, *ApJ*, 610, 663
Oguri, M. & Blandford, R. 2009, *MNRAS*, 392, 930
Paczynski, B. 1986, *ApJ*, 308, L43
Peebles, P. J. E. 1993, “Principles of physical cosmology”, Prince-
ton Series in Physics, Princeton, NJ: Princeton University
Press
Perna, R., Sari, R. & Frail, D. 2003, *ApJ*, 594, 379
Piran, T. 2000, *Phys. Rep.*, 333, 529
Porciani, C. & Madau, P. 2001, *ApJ*, 548, 522
Proga, D., Stone, J. M., & Kallman, T. R. 2000, 2000, *ApJ*, 613,
686
Richards, G. T., et al. 2004, *ApJ*, 610, 679
Rozo, E., Nagai, D., Keeton, C., & Kravtsov, A. 2008, *ApJ*, 687,
22
Spergel, D. et al. 2007, *ApJS*, 170, 377
Takahashi, R., & Chiba, T. 2001, *ApJ*, 563, 489
Warren, M. S., Abazajian, K., Holz, D. E., Teodoro, L. 2006, *ApJ*,
646, 881
Winn, J. N., Rusin, D., & Kochanek, C. S., 2004, *Nature*, 427,
613